Thermokinetic Modeling of Phase Transformation in the Laser Powder Deposition Process

EHSAN FOROOZMEHR and RADOVAN KOVACEVIC

A “nite element model coupled with a thermokinetic model is developed to predict the phase transformation of the laser deposition of AISI 4140 on a substrate with the same material. Four di erent deposition patterns, long-bead, short-bead, spiral-in, and spiral-out, are used to cover a similar area. Using a “nite element model, the temperature history of the laser powder deposition (LPD) process is determined. The martensite transformation as well as martensite tempering is considered to calculate the “nal fraction of martensite, ferrite, cementite, carbide, and retained austenite. Comparing the surface hardness topography of di erent patterns reveals that path planning is a critical parameter in laser surface modi“cation. The predicted results are in a close agreement with the experimental results.

DOI: 10.1007/s11661-009-9870-9

I. INTRODUCTION

LASER powder deposition (LPD) in the past two decades has been one of the fastest growing manufacturing processes. Various applications such as building components with complex geometry, syntheses of functionally graded materials, surface coating, and alloying, and repairing valued components have made it a unique processing technique in manufacturing. Locally heating and cooling the material during the process has serious e ects on the quality of the deposited material. Kaplan and Groboth[1] analytically studied the e ect of parameters on clad layer formation and overlapping of tracks. Labudovic *et al.*[2] studied the e ect of process parameters on the formation of residual stress along the height of a single wall deposition. Choi *et al.*[3,4] had an extensive experimental study on the e ect of laser power, laser scanning speed, and powder ”ow rate on the geometry, microstructure, and defect formation in the process. The studies of the process have shown that the microstructure depends not only on the already mentioned parameters, but also on any parameter that can change the temperature history of each location throughout the buildup. Costa *et al.* has studied the e ect of idle time between layers[5,6] and substrate size[6,7] on the “nal microstructure and hardness of the deposition of a single wall. Similar work was performed by Wang *et al.*[8] to investigate the e ect of laser power and traverse speed on the phase transformation during the process. Kelly *et al.*[9] studied the e ect of the number of layers in depositing a single wall of a type of titanium alloy on the microstructure evolution. More detailed research has also been performed on de“ning the e ect of process parameters on phase transformation during the heat treatment of materials.[10–12] Obviously, reaching a speci“c microstructure or hardness level in the buildup requires understanding of the temperature-phase transformation relation.

A wide range of metal alloys have been used in the LPD process. Depending on the composition of the material, the microstructure transformation may have di erent responses to the process parameters. In the current work, a type of low-alloy steel, AISI 4140, is used to cover the surface of a substrate with di erent deposition patterns. Solid-state phase transformation is de“ned by the temperature and heating or cooling rate. The molten deposited material after solidi“cation at solidus temperature consists of austenite (γ). If the cooling rate is high enough, the martensite transformation, which is a nondi usive transformation, occurs. The minimum required cooling rate for transforming austenite to martensite for AISI 4140 is about 25°C/s.[13] On the other side, the cooling rate in the LPD process is usually much higher than 25°C/s (on the order of 10^4 °C/s[11]) because of a relatively large cold substrate. Therefore, the austenite by crossing the martensite start temperature (M_s) transforms to martensite until it reaches the martensite end temperature (M_f). If the cooling process stops, the martensite transformation also stops and the martensite is transformed only if the temperature continues to cool.[14] The multipass deposition process disturbs the normal cooling trend of the material and may temper the martensite. Tempering the martensite generally has three steps: generation of transition carbides (100°C to 250 °C), transforming retained austenite to ferrite and cementite (200°C to 300 °C), and replacing the transition carbides with cementite and ferrite (starting from 250°C to 350 °C). There might be a forth step for high-alloy steels where alloy carbides are generated at 500°C to 650 °C. This step can be ignored for low-alloy steels such as AISI 4140.

At a new heating cycle, the material may have three conditions: if the material is heated more than A_{c3}, the

EHSAN FOROOZMEHR, Ph.D. Candidate, and RADOVAN KOVACEVIC, Director, are with the Center for Laser Aided Manufacturing (CLAM), Southern Methodist University, Dallas, TX 75205. Contact e-mail: kovacevi@engr.smu.edu
Manuscript submitted October 13, 2008.
Article published online June 24, 2009

material is fully austenitized, and in the next cooling cycle can be transformed to martensite; for temperatures between A_{c1} and A_{c3}, partial austenite is generated so that no austenization at A_{c1} and full austenization at A_{c3} are considered. For temperatures less than A_{c1}, no austenization occurs and the material is tempered. The "nal fraction of each phase of the material at any location de"nes the hardness at that location by considering the hardness of individual phases.

In the surface repairing processes, one of the key parameters that a ects the quality of the "nal part besides the main process parameters is the path planning.[15] Heating and cooling cycles can be changed signi"cantly by changing the surface scanning path. In this study, the e ect of four di erent patterns on the "nal surface hardness of the deposition of AISI 4140 on a substrate with the same material is studied. A coupled thermal and kinetic analysis is employed to calculate the thermal history and hardness throughout the part.

II. PHASE TRANSFORMATION ANALYSIS

Analyzing the phase transformation in the LPD process requires knowledge of the temperature history at each point. The transient nature of the process, in addition to the dependency of material properties on temperature, makes solving the equations analytically impossible. ANSYS "nite element software is used to model the heat transfer during the LPD process. The element ••birth and death•• option in ANSYS is used to model the additive nature of the process. The temperature, as a function of location and time, for each point is used in a subroutine developed in the MATLAB to analyze the phase transformation and "nal microstructure. A semiempirical model is used to identify the fraction of each phase at each point and its corresponding hardness.

A. *Thermal Model*

The "nite element analysis of the temperature of the LPD process with respect to time and location requires the geometry of the part, which is de"ned by a mesh of "nite elements that should be updated over time to represent the additive nature of the process. The continuous movement of the laser beam over the substrate is divided into small divisions of the static thermal analysis, called time-steps.

1. *Mathematical description*

In every time-step, the energy balance equation (Eq. [1]) is solved using the "nite element method, and the results are used as the initial conditions for the next time-step:

$$\mathrm{q}c_p\frac{\partial T}{\partial t} = \nabla\cdot(k\nabla T) \qquad [1]$$

In this equation, q, k, and c_p are density, thermal conductivity, and speci"c heat, respectively. The thermal behavior of the material is de"ned by specifying the temperature-dependent speci"c heat and thermal conductivity as well as the density of the material. The latent heat e ect due to phase transformation is considered in the de"nition of speci"c heat[16] (Table I).

2. *Boundary conditions*

To obtain the solution for the thermal equilibrium equation, the boundary conditions and initial conditions are de"ned. The substrate temperature is equal to T_0 = 25 °C (298 K) at the beginning of the process:

$$T(x, y, z, 0) = T_0 \quad \text{for } (x, y, z) \in \text{substrate} \qquad [2]$$

The heat source boundary condition is considered to be a combination of a heat "ux boundary condition for the leading half of the laser beam spot that heats the substrate in front of the laser beam, and a constant melting temperature for the activated element at the activation time for the trailing half of the laser beam spot that represents the melted deposited material (Figures 2 and 3). The laser beam intensity exposed to the molten pool has Gaussian distribution in the TEM $_{00}$ mode:

$$I = \frac{2\mathrm{a}P}{\mathrm{p}r_b^2}\exp\left(-\frac{2r^2}{r_b^2}\right) \qquad [3]$$

where a is the surface absorption coe cient, P is laser power, r is the radius, and r_b is the laser beam radius, which is de"ned as the radius in which the power density is reduced from the peak value by a factor of e^2. The thermal heat "ux boundary condition for the front half of the beam spot is de"ned by considering the mean value for the Gaussian thermal "ux density of the laser beam:

$$I_{\text{mean}} = \frac{1}{\mathrm{p}r_b^2}\int_0^{r_b} I(2\mathrm{p}r)dr = \frac{0.865\mathrm{a}P}{r_b^2} \qquad [4]$$

The considered value for surface absorption of the Nd:YAG laser is 20 pct.[18] It has been shown by Neto and Vilar[19] that the absorbed energy by "ying powder particles can be su cient for them to reach the melting temperature before entering the molten pool. Therefore, the activated elements at each time-step have the same temperature as the melting temperature:

Table I. Temperature-Dependent Material Properties of AISI 4140[11,17]

Temperature (°C)	25	100	200	400	600	700	800	900	1315	1454	1600
Speci"c heat (J/kg K)	473	473	527	565	723	821	823	624	607	1800	607
Density (kg/m^3)	7760	7760	7650	7600	7580	7550	7200	7150	7100	7000	6900
Conductivity (W/m K)	54.1	51.7	48.6	43.2	38.5	36.5	34.7	33.0	30.1	30.0	30.0

$$T(x,y,z,t_{\text{activation}}) = T_m \quad \text{for } (x,y,z) \in \text{activated elements} \qquad [5]$$

The local surface heat-transfer condition consists of convection heat transfer and radiation:

$$q = h(T_w - T_0) + \varepsilon\sigma\left(T_W^4 - T_0^4\right) \qquad [6]$$

where h is the convection coefficient, ε is the emissivity coefficient, σ is the Stefan–Boltzmann constant, and T_w and T_0 are the surface and ambient temperatures, respectively.

Because the radiation is most effective at high temperatures, this boundary condition is defined only at the molten pool region. In order to reduce the order of nonlinearity of the problem, the local surface heat transfer at the molten pool is estimated according to Vinokurov:[20]

$$q = \left(h + \varepsilon\sigma\left(T^3 + T_0T^2 + T_0^2T + T_0^3\right)\right)(T - T_0) = H_{\text{lump}}(T - T_0) \qquad [7]$$

where H_{lump} can be estimated as

$$H_{\text{lump}} = 2.4 \times 10^{-3}\varepsilon T_m^{1.61} \qquad [8]$$

The associated loss in accuracy using this relationship is estimated to be less than 5 pct.[2] The emissivity coefficient around the melting temperature is considered to be 0.6.[16]

3. *Assumptions*

The assumptions during the thermal modeling of the LPD process are as follows.

(1) The substrate is initially at room temperature (25 °C). The boundary condition around the substrate is the convection heat transfer with a constant coefficient.
(2) The heat flux on the leading half (Figure 2) has uniform distribution, based on Eq. [5].
(3) The latent heat is considered in the temperature-dependent definition of specific heat.
(4) The activated elements of the molten pool are at the melting temperature. The convective redistribution of heat in the molten pool is ignored.

B. *Thermokinetic Model*

Based on the results from the thermal model, the temperature history of the nodes is used to predict the phase transformations during the heating and cooling cycles. The microstructure of the material after solidification consists of austenite. Depending on the cooling rate of the process, different phases can be transformed from the austenite. However, in the LPD process, the high cooling rate due to a large low-temperature mass of substrate results in only a martensite transformation when the temperature drops below M_s.[8] The proportion of martensite in this transformation can be obtained from an empirical relation proposed by Koistinen and Marburger:[21]

$$f_m = 1 - f_c\exp(-0.011(M_s - T)) \quad M_s > T > M_f \qquad [9]$$

where f_c is the fraction of austenite and M_f is martensite end-transformation temperature. The maximum martensite can be achieved when the material cools to reach M_f. In the multipass LPD process, the cooling cycle may be disturbed by the next deposited bead that consequently stops the martensite transformation. Depending on the temperature in the new heating cycle, the martensite may be decomposed to new phases. The following assumptions are used to quantify the tempered microstructure.

(1) The tempering process takes place if there exists any fraction of martensite and the temperature is below A_{c1} and higher than 100°C.
(2) Two steps are considered for the tempering:[11,22]
(a) formation of transition carbide (ε-carbide) and ferrite that occurs during tempering up to 250°C; and
(b) formation of cementite and ferrite that occurs from 250 °C up to A_{c1}.
(3) If the temperature goes higher than A_{c1}, the fraction of austenite linearly increases until it becomes equal to one at A_{c3}.

The fraction of tempered martensite can be calculated with the Johnson–Mehl–Avrami equation for solid-state transformation:[23]

$$f = 1 - \exp(-\beta^n) \qquad [10]$$

where, for the nonisothermal condition,

$$\beta = \int k(T)dt = \int k_0\exp\left(-\frac{Q}{RT}\right)dt \qquad [11]$$

where Q is the martensite tempering activation energy, R is the universal gas constant, and n and k_0 are empirical constants. At any temperature, the fraction of tempered martensite is calculated. The considerable tempered phases are ε-carbide (ε), ferrite (α), cementite (c), and retained austenite (γ_R). As mentioned, martensite transforms to ε-carbide and ferrite at temperatures under 250°C. The amount of untempered martensite (f_{mu}) can be calculated from

$$f_{m_u} = f_m(1 - f) \qquad [12]$$

where f_m is the initial fraction of martensite.

The carbon mass balance for this situation can be represented by

$$C_{\text{material}} = f_{m_u}C_m + f_\alpha C_\alpha + f_\varepsilon C_\varepsilon + f_{cR}C_{cR} \qquad [13]$$

The carbon content of martensite up to 2 wt pct carbon content is the same as the base material.[24] Therefore,

$$C_{\text{material}} = C_m = C_{cR} \qquad [14]$$

and

$$f_m + f_{cR} = 1 \qquad [15]$$

By substituting Eqs. [12], [14], and [15] into Eq. [13] and simplifying the relation, the fraction of ferrite and ε-carbide is defined as

$$f_{\varepsilon} = ff_m \frac{c_m - c_a}{c_{\varepsilon} - c_a} \quad [16]$$

$$f_a = ff_m - f_{\varepsilon} \quad [17]$$

For the temperature between 250 °C and A_{c1}, with a similar calculation, the fraction of cementite and ferrite can be expressed as

$$f_c = ff_m \frac{c_m - c_a}{c_c - c_a} \quad [18]$$

$$f_a = ff_m - f_c \quad [19]$$

After the fraction of each phase in the material is calculated, the hardness of the material can be obtained by considering the fraction of each phase multiplied by its corresponding hardness:

$$H = f_{mu} H_m + f_{\varepsilon} H_{\varepsilon} + f_a H_a + f_c H_c + f_{cR} H_c \quad [20]$$

The assumed values for the parameters used in the modeling are summarized in Table II.

C. *Material Properties*

As mentioned, the fraction of each phase at any point depends on the temperature history with respect to the transformation temperatures M_s, M_f, A_{c1}, and A_{c3}. Because the phase transformation is a diffusive process, it requires enough time to be accomplished. In the LPD process, the heating and cooling rates are on the order of 10^3 to 10^4 °C/s. Extensive research was performed by Miokovic *et al.*[12,25] on the effect of heating and cooling rates on transformation temperatures. Based on their results, the assumed values for A_{c1} and A_{c3} are 850 °C and 925 °C, respectively. This effect, however, for M_s and M_f is negligible, and the assumed values for the martensite start and end temperatures are 350 °C and 150 °C, respectively.

Table II. Assumed Parameters Values in the Modeling Equations [11], [12], [14], [16], and [18]

Parameter	Description	Value
a	surface absorption	0.2
ε	surface emissivity	0.6
A_{c1}	austenization start temperature (°C)	850
A_{c3}	austenization end temperature (°C)	925
C_a	ferrite carbon content	0.015
C_{ε}	ε-carbide carbon content	8.23
C_c	austenite carbon content	0.4
C_C	cementite carbon content	6.7
C_m	martensite carbon content	0.4
H_a	ferrite hardness (HV)	150
H_{ε}	ε-carbide hardness (HV)	600
H_c	austenite hardness (HV)	150
H_C	cementite hardness (HV)	400
H_m	martensite hardness (HV)	700
k_0	empirical parameter (s^{-1})	5.11×10^9
M_f	martensite transformation end temperature (°C)	150
M_s	martensite transformation start temperature (°C)	250
P	laser power (W)	275
Q	activation energy (kJ/mol)	196.9
R	universal gas constant (J/mol K)	8.314
r_b	laser beam radius (mm)	0.5
T_0	ambient temperature (°C)	25
T_m	melting temperature (°C)	1475

III. MODEL APPLICATION

The mentioned coupled models of thermal and thermokinetic analysis are used to investigate the effect of path planning on the microstructure of the deposited material in the LPD process. For this purpose, four cases with the same deposition area are studied for different deposition patterns, as shown in Figure 1.

In the LPD process, as shown in Figure 2, the deposition region can be divided into two regions: the "leading half," which moves in front of the laser beam and melts the substrate; and the "trailing half," which follows the leading half and contains the molten material. This concept is used for modeling the deposition process by the finite element method, as shown in Figure 3. In this figure, four regions are distinguished: the white elements represent the substrate or the layer underneath, the light-gray elements represent the deposited elements that were activated in the previous time-steps, the dark-gray elements are the activated elements

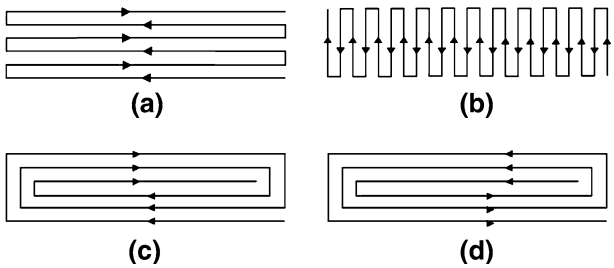

Fig. 1—Schematic presentation of deposition paths: (*a*) long-beads, (*b*) short-beads, (*c*) spiral-in, and (*d*) spiral-out.

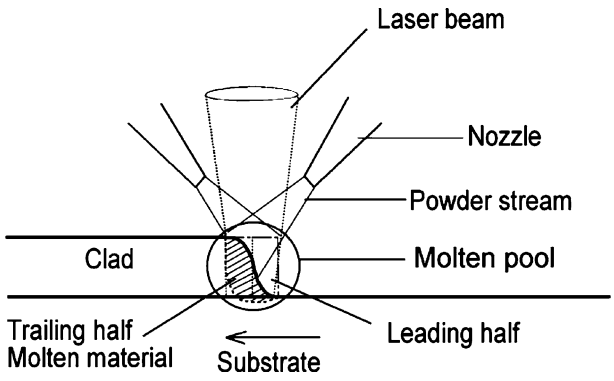

Fig. 2—Schematic of LPD process, leading half and trailing half are shown in the molten region.

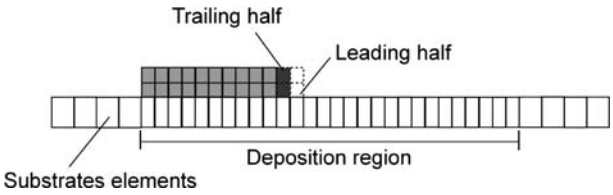

Fig. 3—Finite element model for the LPD process.

in the current time-step and have the boundary condition melting temperature, and the dotted region represents the leading half in which the heat flux is activated on the substrate in the current time-step. Therefore, in every time-step, the heat flux is activated on the element of the substrate or previous layer followed by the activation of the elements having the boundary condition of melting temperature. The process continues until the total length of one bead is completed. Then, the beam changes direction to follow the path, as shown in Figure 1. The coating is complete when the corresponding path is finished. The deposition process is followed by a cooling time until the part cools to room temperature.

In the present study, the laser scanning speed is 10 mm/s, and the powder feeding rate is 3 g/min with a powder efficiency of 30 pct. The deposition area, as shown in Figure 4, is 15×5 mm, and the spacing between deposition tracks is 0.5 mm. With a time-step of 25 ms, a set of four elements of $0.25 \times 0.25 \times 0.20$ mm dimension is activated (Figure 4). The area on which the heat flux is activated is 0.25×0.50 mm^2.

IV. RESULTS AND DISCUSSION

The obtained results from the model show that the deposition pattern has a strong effect on the final hardness of the surface. This effect is shown in Figures 5 through 8 for the long-bead, short-bead, spiral-in, and spiral-out patterns, respectively. In each figure, the corresponding deposition path is shown. For the long-bead pattern, as shown in Figure 5, the hardness has a minimum value at the starting bead and a maximum value at the last two beads. In between the starting and ending edges, the hardness has a fairly uniform distribution with a smaller value than the maximum hardness, except at the end points of each bead. The short-bead pattern, however, has a significantly different hardness distribution. Although the first bead shows a

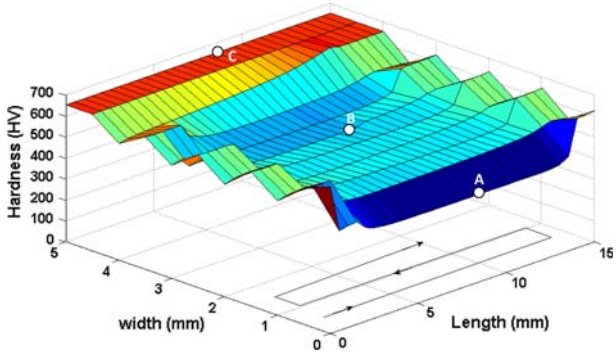

Fig. 5—Surface hardness topography of long-bead pattern.

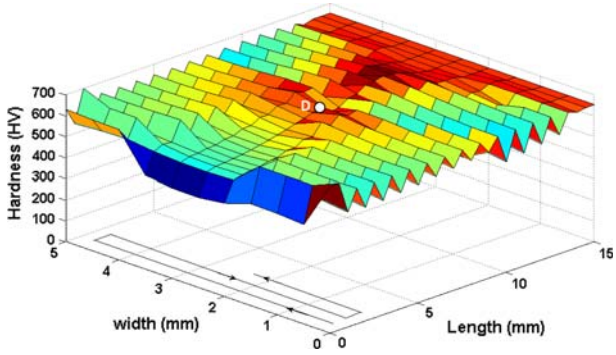

Fig. 6—Surface hardness topography of short-bead pattern.

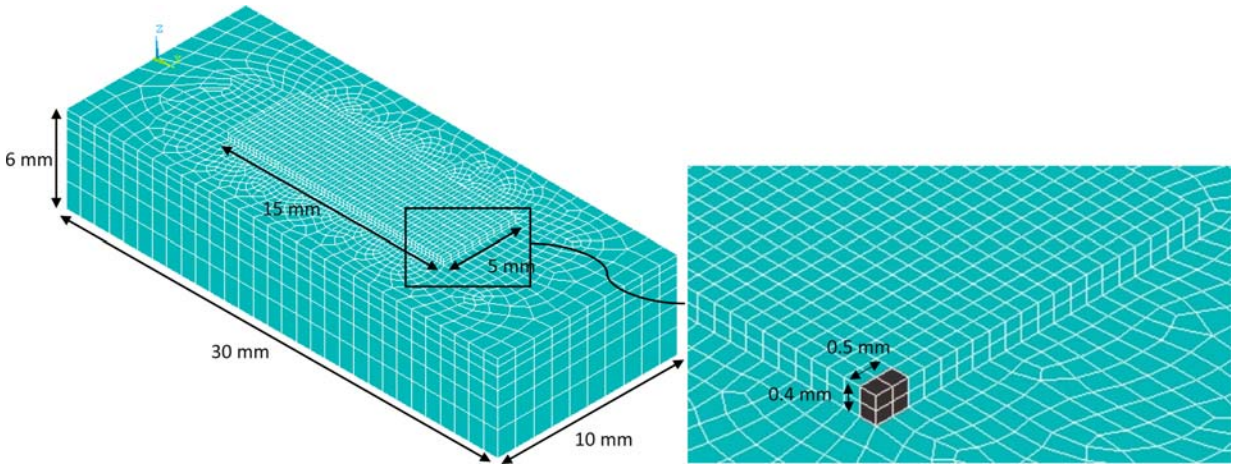

Fig. 4—Finite element model of the substrate and deposition region for one-layer cladding; the first activated set of elements is shown in a higher magnification.

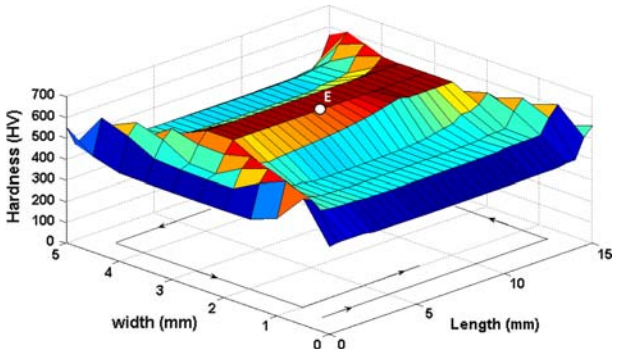

Fig. 7—Surface hardness topography of spiral-in pattern.

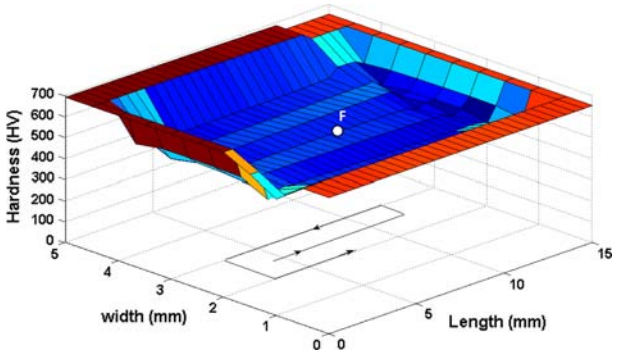

Fig. 8—Surface hardness topography for spiral-out pattern.

relatively low hardness, the other beads up to the last few beads have fairly uniform and high hardness values. The last few beads have a maximum hardness.

The spiral-in and spiral-out patterns, as shown in Figures 7 and 8, have a symmetrical distribution of hardness along the longitudinal and traversal mid-axes. Nonetheless, the spiral-in pattern has an increasing trend from the outer edges to the center, while the spiral-out pattern has a decreasing trend from the outer edges to the center. An overview of the four mentioned cases reveals that the starting region of the deposition path has the smallest hardness and the ending region of deposition has its maximum value. This result is in agreement with similar observations reported by Costa *et al.*,[5..7] Wang *et al.*,[8] and Kadiri *et al.*[26] in the deposition of a single wall.

Referring back to Figure 5, three points (A, B, and C) at the center line of the length of the surface are located at the center of the "rst, middle, and last beads, respectively. The temperature, austenite fraction, and hardness *vs* time for these points are shown in Figure 9. For point A, the second peak temperature (marked with a in Figure 9(a)) does not cross the A_{c1} line, and no new austenite is generated (point a' in Figure 9(b)). However, this high temperature tempers the material and causes a reduction in the corresponding hardness (marked with a'' in Figure 9(c)). The temperature pro"le for point B shows a high peak value for the second heating cycle (marked with b in Figure 9(a)) that results in full austenization of the material (point b' in Figure 9(b)). Consequently, the hardness drops to the austenite hardness level (point b'' in Figure 9(c)). The third peak (c) results in tempering the material and a reduction in the hardness pro"le (marked with c''). Because the tempering temperature (point c in Figure 9(a)) for point B is less than the tempering temperature (point a in Figure 9(a)) for point A, less reduction in hardness is observed (point c'' *vs* point a''). Point C, however, does not experience any tempering cycle. Therefore, the maximum hardness is expected for this point. The retained austenite fraction for points A and B is negligible, as shown in Figure 9(a). However, at point C, the retained austenite fraction is about 11 pct. This prediction of the model about a higher value for retained austenite for untempered locations in the laser deposition process is in agreement with the results reported in References 6, 8, 17, and 27.

The center nodes of the experiments shown in Figures 6 through 8 are marked with letters D, E, and F, respectively. The results of studying the e ect of the deposition pattern on the phase transformation during the LPD process are shown in Figure 10. Point D, as shown in Figure 10(a), has shorter heating cycles than points E and F, due to the shorter traveling path of the laser beam. After the second peak temperature in point D, a small amount of martensite is formed by decreasing the temperature to a point marked with a in Figure 10(a). Consequently, an increase in the hardness (marked with a'' in Figure 10(c)) and a decrease in the austenite fraction (marked with a' in Figure 10(b)) occur at the corresponding time. The next peak temperature is marked with b in Figure 10(a). Because the amount of transformed martensite in the last cooling cycle is very small, this tempering cycle is not very e ective in reducing the hardness at the corresponding time. In addition, the amount of retained austenite is high enough to be transformed to martensite in the next cooling cycle that crosses M_s. The next peak temperatures coming after point b are relatively low and do not have a noticeable e ect on reducing hardness. Therefore, a progressive trend in the hardness of this point is observed up to the end of the process.

Point E in Figure 10 has a similar thermal history to point C in Figure 9. Because point E is on the last deposition bead, there is no tempering cycle after cooling the point under M_s. Therefore, the highest achievable hardness is expected at this point. Point F in Figure 10 is also similar to point B in Figure 9. The "rst peak temperature below the A_{c1} (marked with c in Figure 10(a)) tempers the material and causes a reduction in the corresponding hardness (marked with c'' in Figure 10(c)). Because the retained austenite at this point (marked with c' in Figure 10(b)) is relatively small, cooling the material to the point marked with d slightly increases the hardness.

Considering the fact that all process parameters are kept constant during the experiments, the signi"cance of selecting the deposition pattern is obvious by comparing the results shown in Figures 5 through 8. The four di erent deposition patterns have a di erent tempering e ect on the previously deposited beads. If the bead number is indicated by m, the deposition of the bead m

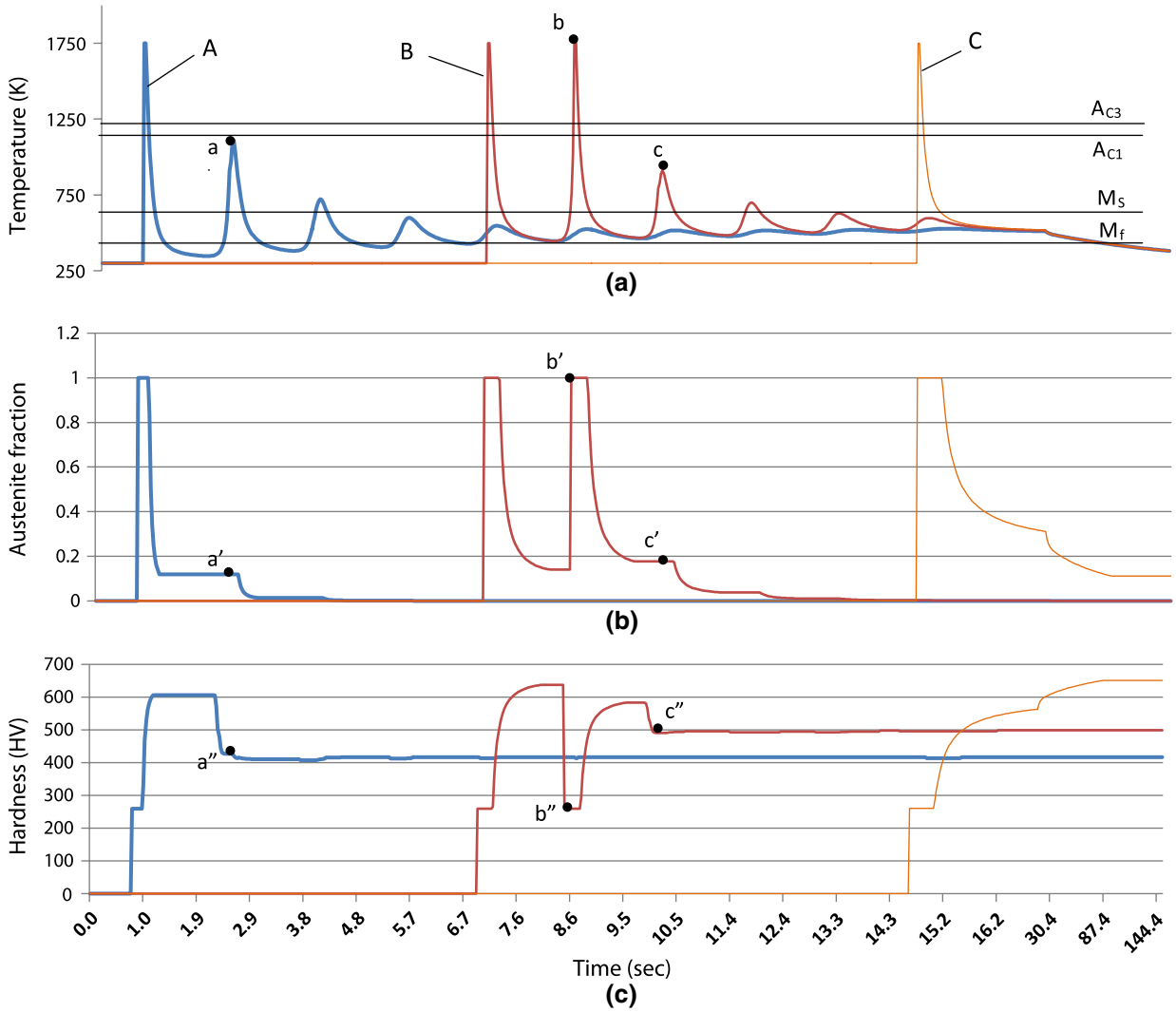

Fig. 9—(*a*) Temperature, (*b*) austenite fraction, and (*c*) hardness *vs* time for Fig. 5, points *A*, *B*, and *C*.

results in full austenization of bead $m-1$ and tempering bead $m-2$. The time interval between the deposition of beads $m-1$ and m is the result of choosing the deposition path. As shown in Figure 10(a), the tempering time interval (Δt_2) for the short-bead pattern at point D (shown in Figure 6) is about one-third of the one (Δt_1) for the spiral-out pattern at point F (shown in Figure 8). This larger time results in a larger decrease in the temperature at point e, which is even less than M_f. Consequently, the austenite fraction drops equal to Δc_1 in Figure 10(b). However, the minimum temperature marked with a results in a reduction of austenite equal to Δc_2 in Figure 10(b). A greater decrease in the bead deposition interval can even eliminate any formation of martensite. Nonetheless, the deposition area could be a limitation in choosing the optimal deposition pattern. The obtained results show that the short-bead experiment has a higher average and reasonably uniform hardness. The spiral-out and long-bead patterns also show a relatively uniform hardness distribution away from the edges, although the average hardness for the mentioned patterns is noticeably less than the short-bead pattern. The spiral-in pattern has the most nonuniform hardness distribution.

V. MODEL VERIFICATION

In order to verify the validation of the model, a series of experiments are performed. The experimental setup comprises a 1-kW continuous wave Nd:YAG laser system with a deposition head, a 5-axis CNC vertical machining center, and a powder feeding system with argon carrying gas. Each coupon is clamped on the CNC table before performing the experiment. Each deposition path is de“ned in the CNC machine with the same process parameters as the model (laser power, laser scanning speed, and spacing between tracks). Figure 11 shows the coupons for di erent deposition patterns. To compare the surface hardness of the coupons with the modeled hardness values shown in Figures 5 through 8, the coupons are ground slightly and polished to become smooth enough for the microhardness test. A 200-g load and 150-l m distance between indentations are chosen

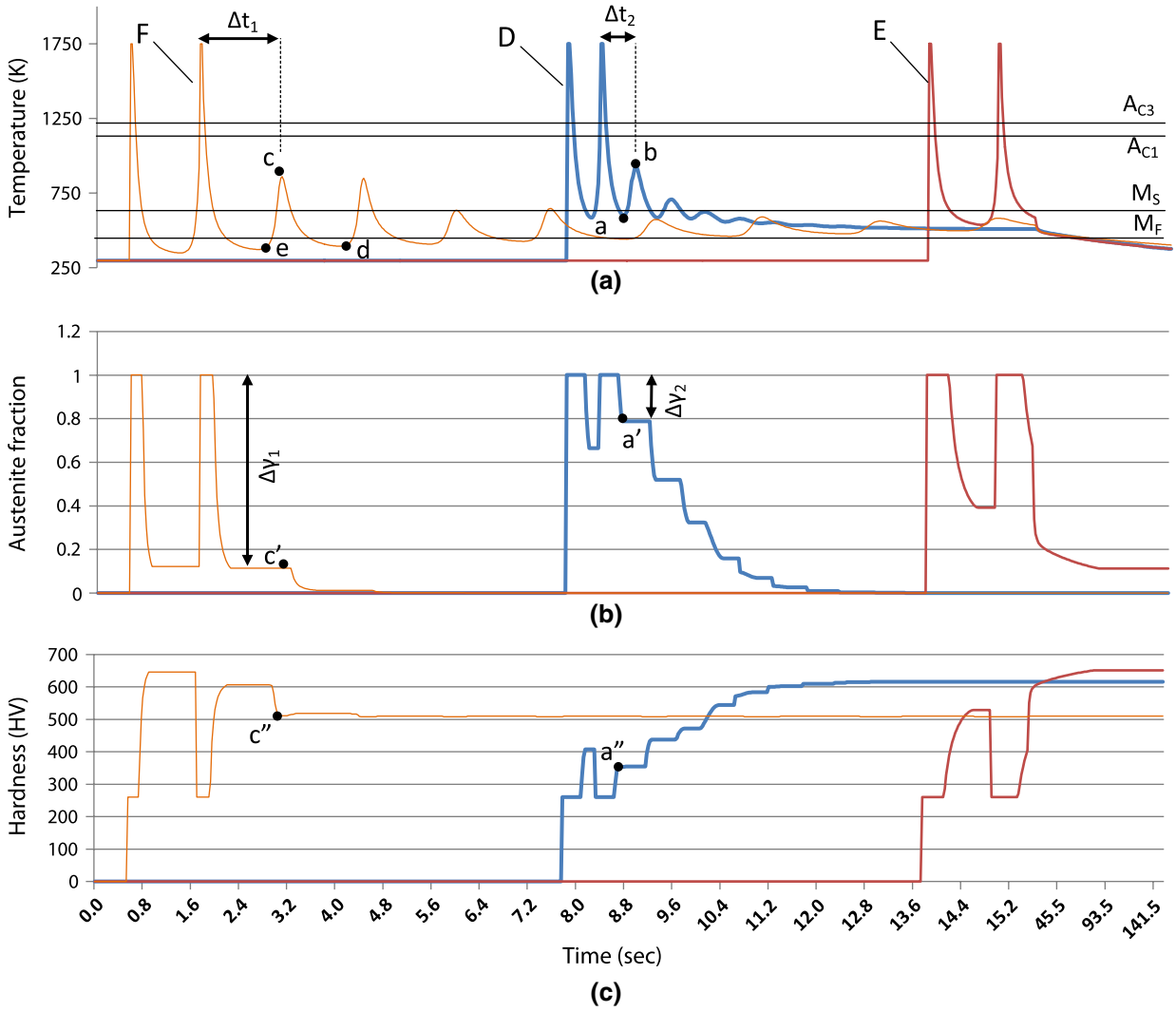

Fig. 10„(*a*) Temperature, (*b*) austenite fraction, and (*c*) hardness*vs* time for the Figs. 6 through 8, points *D*, *E*, and *F*.

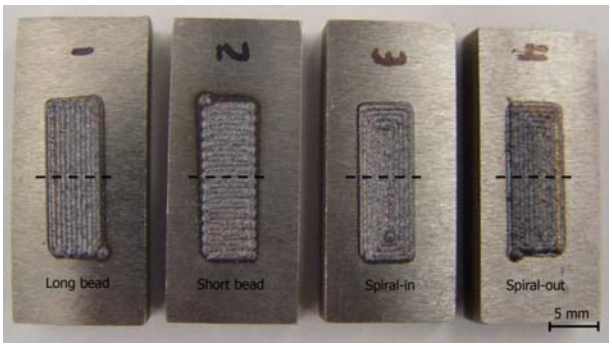

Fig. 11„Experiments performed under di erent deposition paths.

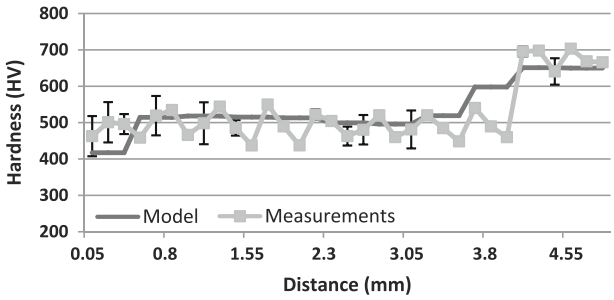

Fig. 12„Measured and predicted hardness along the central traverse line for long-bead pattern.

for the microhardness test experiments. Along the traverse line at the center of the coupons (dashed lines shown in Figure 11) and from left to right, two series of measurements are performed for each coupon, and the results are compared with the model predictions, as shown in Figures 12 through 15.

The measured hardness values are in a very good agreement with the predicted ones in the model. The measurements shown in Figure 12 reveal that the hardness has a relatively uniform distribution except for the last two beads. The topography of hardness shown in Figure 5 clearly shows this trend. The short-bead pattern shown in Figure 13, however, has a

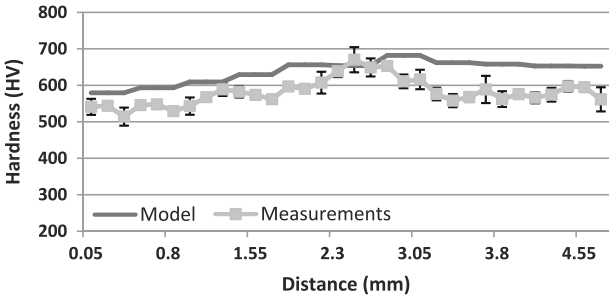

Fig. 13„Measured and predicted hardness along the central traverse line for short-bead pattern.

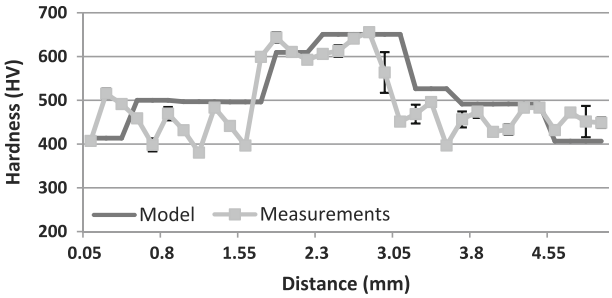

Fig. 14„Measured and predicted hardness along the central traverse line for spiral-in pattern.

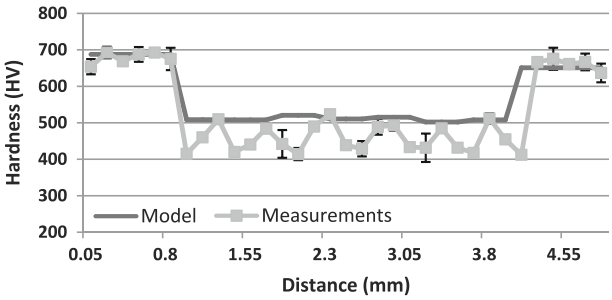

Fig. 15„Measured and predicted hardness along the central traverse line for spiral-out pattern.

relatively smooth hardness variation with an average value of about 60 to 80 HV higher than that of other patterns. The experimental results for the spiral-in and spiral-out patterns follow the expected variations, as shown in Figures 7 and 8.

VI. CONCLUSIONS

The thermokinetic model of the LPD process can be e ectively used to predict the e ect of process parameters on the “nal microstructure of the buildup. In the present work, this model is used to study the e ect of path planning on the “nal hardness of the surface. It is shown that the deposition path can in”uence the temperature history of di erent points and can a ect the “nal microstructure of the part. Among four di erent deposition patterns covering a similar area, the short-bead pattern shows a higher average hardness. However, the spiral-in pattern has the most nonuniform hardness distribution. The long-bead and spiral-out patterns end up with a relatively uniform hardness distribution but less hardness than the short-bead pattern. The experimental results show a very good agreement with the predicted values of the model.

ACKNOWLEDGMENT

This project was “nancially supported by NSF Grant No. EEC-0541952.

REFERENCES

1. A.F.H. Kaplan and G. Groboth: *J. Manuf. Sci. Eng. Trans. ASME*, 2001, vol. 123, pp. 609…14.
2. M. Labudovic, D. Hu, and R. Kovacevic: *J. Mater. Sci.*, 2003, vol. 38, pp. 35…49.
3. J. Choi and Y. Chang: *Int. J. Mach. Tools. Manuf.*, 2004, vol. 45, pp. 597…607.
4. J. Choi and Y. Hua: *J. Laser Appl.*, 2004, vol. 16(4), pp. 245…51.
5. L. Costa, T. Reti, AM. Deus, and R. Vilar: *Proc. Int. Conf. Metal Powder Deposition for Rapid Manufacturing*, Princeton, NJ, 2002, pp. 172…79.
6. L. Costa, R. Vilar, T. Reti, and A.M. Deus: *Acta Mater.*, 2005, vol. 53, pp. 3987…99.
7. L. Costa, R. Vilar, T. Reti, R. Colaco, A.M. Deus, and I. Felde: *Mater. Sci. Forum*, 2005, vols. 437…474, pp. 315…20.
8. L. Wang and S. Felicelli: *Manuf. Sci. Eng. Trans. ASME*, 2007, vol. 129, pp. 1028…34.
9. S.M. Kelly, S.S. Babu, S.A. David, T. Zacharia, and S.L. Kampe: *TMS 2004*, Charlotte, NC, pp. 45…52.
10. C.C. Liu, X.J. Xu, and Z. Liu: *Finite Elem. Anal. Des.*, 2003, vol. 39, pp. 1053…70.
11. R.S. Lakhkar, Y.C. Shin, and M.J.M. Krane: *Mater. Sci. Eng. A*, 2008, vol. 480, pp. 209…17.
12. T. Miokovic, V. Schulze, O. Vohringer, and D. Lohe: *Mater. Sci. Eng. A*, 2006, vols. 435…436, pp. 547…55.
13. M. V. Li, D.V. Niebuhr, L.L. Meekisho, and D.G. Atteridge: *Mater. Trans. B, Process Metall. Mater. Process Sci.*, 1998, vol. 29B, pp. 661…72.
14. M.A. Golozar: *Principles and Applications of Heat Treatment of Steels*, Isfahan University of Technology Press, Isfahan, Iran, 2001.
15. G. Wang, Y. Chen, and H. Zhang: *Thin Solid Films*, 2003, vol. 435, pp. 124…30.
16. M. Labudovic, D. Hu, and R. Kovacevic: *Proc. Inst. Mech. Eng. B: J. Eng. Manuf.*, 2000, vol. 214(8), pp. 683…92.
17. L. Wang, H.E. Kadiri, S. Felicelli, M. Horstemeyer, and P. Wang: *SPIE Defense and Security Symp.*, Orlando, FL, 2007.
18. L.R. Migliore: *Adv. Mater. Processes*, 1998, can be accessed at http://www.laserk.com/newsletters/index.html accessed Aug. 2008.
19. O.O.D. Neto and R. Vilar: *J. Laser Appl.*, 2002, vol. 14 (1), pp. 46…51.
20. V.A. Vinokurov: *Welding Stresses and Distortion: Determination and Elimination*, British Library Lending Division, Boston Spa, England, 1977, pp. 118…19.
21. D.P. Koistinen and R.E. Marburger: *Acta Metall.*, 1959, vol. 7, p. 59.
22. K. Davut, C.H. Gur, and X. Kleber: ECNDT 2006, Poster 108.
23. E.J. Mittermeijer: *J. Mater. Sci.*, 1992, vol. 27, pp. 3977…87.
24. G. Krauss: *Steels: Heat Treatment and Processing Principles*, ASM INTERNATIONAL, Materials Park, OH, 1990.
25. T. Miokovic, J. Schwarzer, V. Schulze, O. Vohringer, and D. Lohe: *J. Phys. IV JP.*, 2004, vol. 120, pp. 591…98.
26. H.E. Kadiri, L. Wang, M.F. Horstemeyer, R.S. Yassar, J.T. Berry, S. Felicelli, and P.T. Wang: *Mater. Sci. Eng. A*, 2008, vol. 494 (1…2), pp. 10…20.
27. R. Colaco and R. Vilar: *J. Mater. Sci. Lett.*, 1998, vol. 17, pp. 563…67.